IEEE Access
Multidisciplinary | Rapid Review | Open Access Journal

Received April 10, 2020, accepted April 24, 2020, date of publication May 6, 2020, date of current version May 20, 2020.

Digital Object Identifier 10.1109/ACCESS.2020.2992459

Enhancing the SEM Signature via the Optimum Onset With a Bistatic and Cross-Polarization Radar Configuration

FAISAL F. H. ALDHUBAIB
College of Technological Studies (CTS), The Public Authority for Applied Education and Training (PAAET), Adailiyah 13092, Kuwait
e-mail ff.aldhubaib@paaet.edu.kw

This work was supported by the Public Authority of Education and Training, Research Project under Grant TS-17-14.

ABSTRACT This paper assesses the feasibility of finding a time bin of optimum onset to improve the robustness of the resonance modes of a midsized aircraft target in the context of radar target identification subject to bistatic and polarization diversities. The approach utilizes the frequency data (noncoherent) to determine a reference onset and a reference resonant frequency set of interest and then employs the time data (coherent) to determine an optimum onset that leads to a minimum error between the reference and extractable mode frequencies. Both sets of data are subject to a qualitative assessment to investigate the impact of the bistatic and polarization radar configurations on the optimum onset to improve the mode extraction. The results show that an optimum onset, compared to the reference onset, is more immune to noise perturbation and has a better discriminative ability for same-class targets.

INDEX TERMS Singularity expansion method, radar target identification, bistatic, polarization, feko.

I. INTRODUCTION

Successful automatic target recognition (ATR) of a noncooperative target depends on deriving discriminative physical features from a radar signature model that is robust to perturbations and ambiguities in the radar signal [1]–[7]. Such a signature model is the singularity expansion method (SEM) model, which approximates the late time of the radar echo due to a pulsed incident field as a set of natural resonance modes related to the shapes and dimensions of the target cardinal structures [8]–[11]. However, the robustness of the signature depends on the proper selection of the late-time onset to ensure that the matrix pencil method (MPM) extracts all modes accurately and consistently [12]–[15]. Unfortunately, as a rule of thumb, the late-time onset is dependent on the target dimensions projected along the incident and scattering directions; ambiguity of the late-time onset naturally arises if the target's geometry in a recognition scenario is unknown to the radar system user. Additionally, the late-time response is usually of low energy content, making extraction of the weakly excited modes challenging for some incident directions or polarization states, thus leading to inferior SEM performance.

Previous work notes that the E-pulse technique (introduced by Rothwell *et al*. [16]) in the early time could overcome the problem of weak late-time modes but at the expense of a higher computation burden as the modes become more aspect dependent [17]. Another work suggests reducing the computational burden of the early-time method by first applying the late-time E-pulse method to narrow down the required range of target aspects before applying the early-time E-pulse [18]. However, both works considered cooperative targets in the sense that their geometry is known beforehand; thus, the onset commences after a period of twice the transit time when the wavefront passes the most longitudinal dimension, i.e., farthest tip, of the target plus the pulse duration. In a noncooperative scenario, prior knowledge of the target geometry is not available; therefore, the late-time onset cannot be estimated based solely on the geometry, especially as the onset may considerably vary with changing target aspect, bistatic, and polarization configurations.

Additionally, the E-pulse performance is evaluated only for dissimilar-class targets, i.e., those with different dimensions, without any attempt to apply the method to same-class

The associate editor coordinating the review of this manuscript and approving it for publication was Weimin Huang.

targets, i.e., those with the same dimensions. Hence, using one late-time onset for all different aspect, scattering and polarization configurations leads to suboptimal or even inferior results. Instead, as [19] illustrates, the estimation of the late-time onset could be based solely on analyzing the late-time signal itself by exploiting its singular values in Hankel matrix form. However, this study used a canonical target, i.e., a flat plate, which has a single fundamental mode signature, and the onset estimate was still very sensitive to noise. Previously, the author adopted a reference onset inferred from the frequency of the first peak in the magnitude spectrum of the target radar echo [20]. Then, the author investigated the impact of polarization diversity and bistatic scattering of a single incident pulse on mitigating the onset impact on the SEM signature. In this case, the study assessed the mode distributions for three discrete onsets that occurred before, at, and after the reference onset [21].

Instead, the present approach conducts a more detailed and qualitative assessment of both the frequency (noncoherent) and time (coherent) data, with the aim of determining the optimum onset and its dependency on the bistatic and polarization configurations. Hence, a preliminary evaluation begins first in the frequency domain to obtain reference (ideal) mode frequencies from the magnitude spectrum peak frequencies [20]. Additionally, the frequency assessment seeks to find the bistatic configuration, i.e., four scattering directions per incident direction, that enhances the accuracy and consistency, i.e., extraction quality, of the modes by reviewing the scattering patterns of the ideal mode frequencies. Then, in the time domain, the assessment principally utilizes the mode frequency distribution with onset shift to reveal the frequency error between the extracted frequencies in the time domain and the reference frequencies determined in the frequency domain. As a result, the frequency error distribution reveals the optimum onset with minimum error and the onset bin with minimal error according to a selected error threshold. The assessment also utilizes a variance figure of merit to account for the noise effect by quantifying the resemblance between the signal reconstructed from the estimated modes (extracted by the MPM) and the original noisy signal truncated by the optimum onset. In this context, the simulation utilizes two models of same-class aircraft targets to validate the optimum onset approach in the context of radar target identification.

II. SIMULATION CONFIGURATIONS & SEM MODEL

Utilizing FEKO simulation of a midsized aircraft target, the software calculates the frequency and then synthesizes the time data for different bistatic and polarization directions [22]. Figure 1 depicts the primary target (with dimensions annotated) in free space, namely, model A, with a wing front-sweep of 50°. The benchmark or comparison target, namely, model B, has a wing down-sweep of 20° to benchmark the discriminative ability of the method for the case of same-class targets. The wedged structures, i.e., wing, tail and stabilizer, have dimensions in the half-wavelength equivalent range of 7–24 MHz. Hence, the fundamental mode

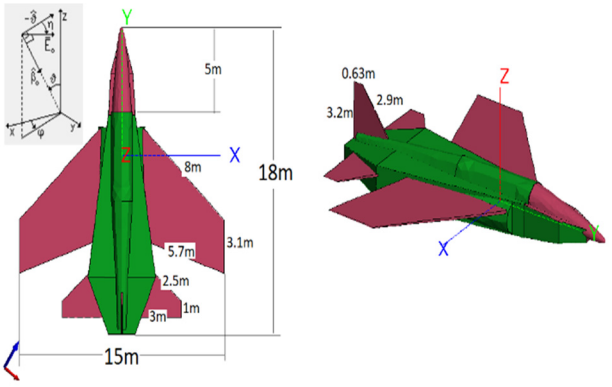

FIGURE 1. The aircraft model. The main frame is made of 0.005 m thick titanium (green).

region extends from the high-frequency (HF) band to the very high frequency (VHF) band for the decade region [4]. The simulation adopts a plane wave excitation of continuous frequency between 0.1 and 50 MHz propagating in the incident direction $\hat{\beta}_{inc}$ with a linear polarization direction, η, towards the coordinate system origin.

The incident vector, $\hat{\beta}$, gives the elevation (or Theta) angle, ϑ, from the $z = 0$ axis, and the azimuth (or Phi) angle, φ, from the $x = 0$ axis, while the polarization direction, η=[0, 90°], represents a vertical (V or Theta) direction perpendicular to the azimuth plane and a horizontal (H or Phi) direction parallel to the azimuth plane. The simulation has a scattering setup limited to a set of coarse incident and scattering directions, where a single incident pulse has four scattering directions divided by 90°.

The time data are computed by Fourier transformation of the coherent frequency data and then convolution with an unmodulated Gaussian pulse to synthesize the baseband excitation necessary to excite the fundamental modes in the HF band only. A Gaussian pulse, u, of interpulse period t_d, peak amplitude u_o, pulse delay t_o, and pulse width p_w can be expressed as follows:

$$u(t) = u_o e^{-\left(\frac{2\sqrt{\ln(2)}}{p_w}\right)^2 (t-t_0)^2}, \quad 0 \le t < t_d \tag{1}$$

Then, the overall time signal, y, consists of early and late time parts (see Figure 5, for example). Thus, truncating the whole-time signal by a unit step function shifted by a time onset, T_l, will create a truncated (late time) signal, y_l, as follows:

$$y_l(t) = y(t) \cdot \delta(t - T_l) \tag{2}$$

Now, applying the MPM to the truncated signal yields a mode series described by a natural frequency, ω, a decay factor, σ, and a residue, a, with error variance ε_n. Hence, the signal reconstructed by the extracted modes, y_{recon}, is expressed as follows:

$$y_{recon}(t) = \sum_{m=1}^{M} a_m . \sin \omega_m t \cdot e^{\sigma_m t} \tag{3}$$

TABLE 1. The simulation configuration.

Symbol	Quantity	Value
f_L	Start Frequency	0.1 MHz
f_H	End Frequency	50 MHz
Δf	Sampling Frequency	779 kHz
ϑ_{inc}	Incident Theta (Elevation)	110°
φ_{inc}	Incident Phi (Azimuth)	[-90:45:90]
φ_{scat}	Scattered Phi	φ_{inc}+[0,90,180,270]
t_d	Interpulse Duration	500 ns
p_w	Pulse Width	20 ns
Δt	Sampling Time	1.95 ns
t_o	Pulse Delay	50 ns
N_p	Number of Pulses	1000
CIT	Coherent Integration Time	0.5 ms

and

$$\varepsilon_n = \mathrm{Var}(y_l - y_{recon}) \tag{4}$$

The order of the modes, M, must be equivalent to the number of cardinal dimensions of interest; thus, for aircraft targets, $M = 4$ is recommended. The complex frequency variable, $\sigma_m + j2\pi f_m$, forms the *mth* mode pole in the Laplace plane, which is target-aspect independent, so it can be considered as a first-layer feature to determine the target class. The mode dominance, $|a/(\sigma/\text{light speed})|$, combines the residue and the damping factor to reflect the degree of mode energy; it can be considered as a second-layer feature to complement the first-layer feature to enhance the discriminative ability of the radar features, particularly in the case of same-class targets [23]. For the noisy time data, the coherent integration time (CIT) can be calculated from the interpulse duration and the number of pulses, N_P, as follows:

$$\mathrm{CIT} = t_d \times N_p \tag{5}$$

Then, the time samples, y_n, are combined into a new whole-time signal,

$$y = \sum_n^{N_p} y_n e^{j\chi_n} \tag{6}$$

The phase weights, $e^{j\chi_n}$, compensate for the phase of the sample signals so that they add in-phase. In free space, i.e., no reflections, it is possible to omit the phase factor and assume that the integrated signals are in phase. Table 1 summarizes the simulation configuration used to calculate the frequency and time data of interest.

III. THE ASSESSMENT METHOD

The method involves conducting a qualitative assessment in the frequency and time domains to derive four quality factors to find the optimum onset and then evaluate its performance.

A. FREQUENCY DATA ASSESSMENT

The preliminary phase in the frequency domain is per incident scattering and polarization configuration of interest (as Table 1 indicates) and involves determining the following:

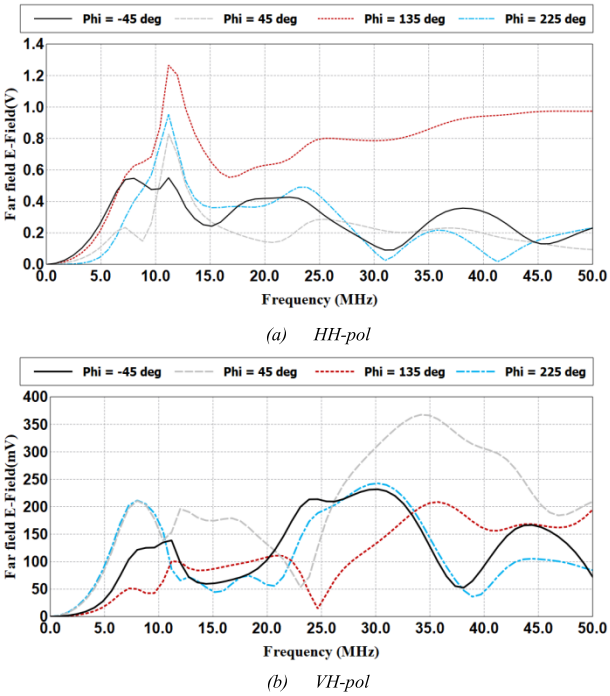

FIGURE 2. The magnitude spectrum per scattering direction (trace1 (▽), trace2 (▷), trace3 (△) and trace 4 (◁)) for incident angle $\varphi_{inc} = -45°$.

step 1) The reference (ideal) frequencies, f'_m, from a set of peak frequencies, f_{max} (see Figure 2 for example) (considering that the equivalent half-wavelength of each reference frequency is comparable to a cardinal dimension of the target class of interest and that their set order is equivalent to the preselected mode order, M).

step 2) The reference onset, T_o, as the first peak frequency reciprocal, $1/f'_1$, plus the pulse width and delay as follows [20]:

$$T_o = p_w + \frac{1}{f'_1} + t_o \tag{7}$$

step 3) The scattering pattern per incident direction of the higher reference frequency (see Figure 3).

step 4) The reference frequency-averaged scattering pattern (see Figure 4) to determine the maximal scattering direction for each incident direction of each reference frequency.

Steps 3-4 serve to review the bistatic configuration that has enhanced returns and thus has a better chance of mitigating the onset effect and improving the mode energy in general.

B. TIME DATA ASSESSMENT

The leading indicator in the time assessment used to assess the quality, i.e., accuracy and consistency, of the mode frequency extraction is the frequency mean squared error (f_{MSE}), obtained by estimating the error between the mode frequencies extracted by the MPM and the reference frequencies

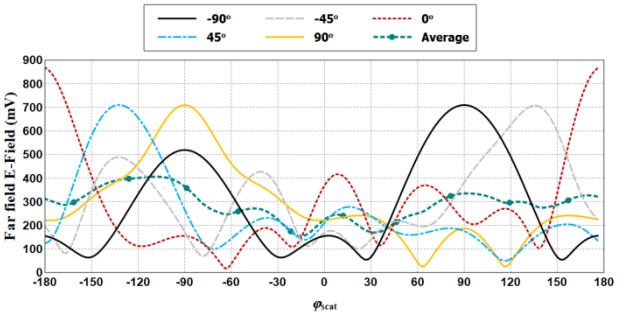

(a) HH-pol

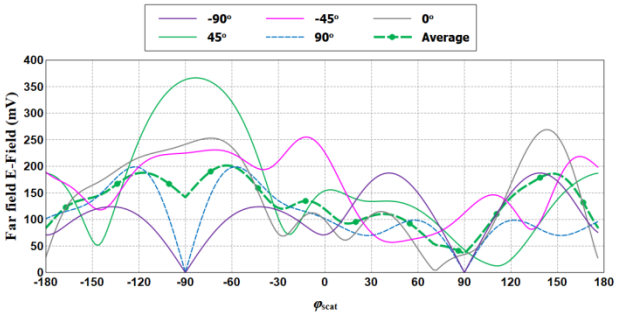

(b) VH-pol

FIGURE 3. The scattering pattern per incident direction of the fourth mode.

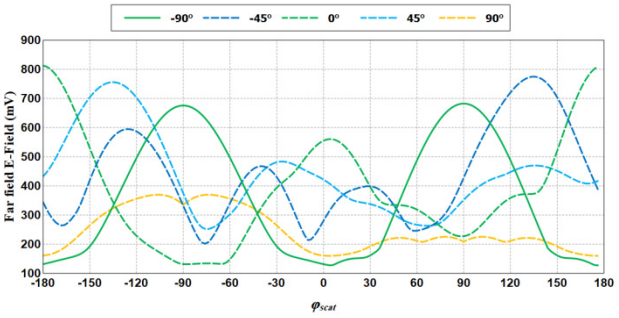

(a) HH-pol

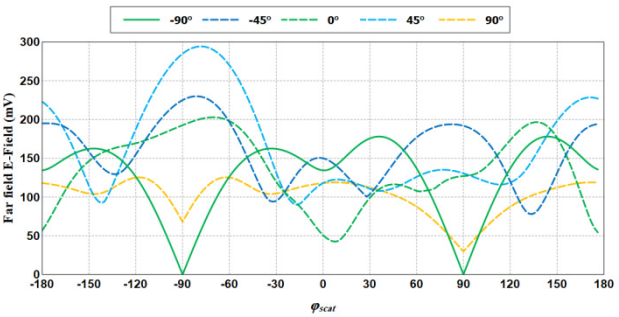

(b) VH-pol

FIGURE 4. The mode-averaged scattering pattern per incident direction.

selected from the magnitude spectrum as follows:

$$f_{MSE} = \frac{1}{M}\sum_{m=1}^{M}(f_m - f'_m)^2 \tag{8}$$

Then, from the leading indicator comes two secondary factors: the first is the minimum error (optimum) onset, T_{MSE}, which corresponds to the time onset when f_{MSE} is at its minimum value, and the second is the minimal onset bin (ΔT_{MSE}), which corresponds to the size (length) of the time bin (duration) when f_{MSE} is below a preset value. To further account for the noise effect on the extracted modes, the fourth indicator, namely, the variance amplitude figure (VAF), quantifies the resemblance between the reconstructed signal and the (noisy) truncated signal as follows:

$$VAF(\%) = \left(1 - \frac{\varepsilon_n}{\mathrm{Var}(y_l)}\right) \times 100 \tag{9}$$

Henceforth, the time domain assessment utilizes the four factors f_{MSE}, T_{MSE}, ΔT_{MSE} and VAF_{MSE} and involves determining the following:

step 1) The mode frequency distribution versus onset to find the optimum onset, T_{MSE}, and the minimal onset bin, ΔT_{MSE} (see Figure 6). (In this case, the minimal f_{MSE} is below 4 MHz^2.)

step 2) The impact of the cross-polarization channel, *i.e.*, *VH-pol*, on the mode distribution (see Figure 7).

step 3) The effect of the optimal onset on the pole (damping versus frequency) estimate compared to the reference onset (see Figure 8).

step 4) The impact of the optimal onset on the dominance factor (for the noiseless case) to discriminate the two models (see Figure 9).

step 5) The noise effect on the four factors (see Table 3) and the dominance factor compared to the reference onset (see Figure 10).

IV. RESULTS & DISCUSSIONS

A. FREQUENCY ANALYSIS (NONCOHERENT DATA)

Let us first begin by assessing the magnitude spectrum to reveal the presumed reference frequencies, as depicted in Figure 2 per the four orthogonal scattering directions (backward ($\triangledown$), rightward ($\triangleright$), forward ($\triangle$), and leftward ($\triangleleft$)) for the incident angle $\varphi_{inc} = -45°$ only. The presumed reference frequencies pertaining to the peaks in the magnitude spectrum are in the vicinities of 7.14, 11, 17.5, and 23 MHz. In the *HH-pol* channel, the peaks in the forward and side (leftward and rightward) directions tend to dominate over those in the backward direction, with the highest peak near the 11 MHz region for the forward direction.

In the *VH*-pol channel, the two side directions, especially the rightward scattering, seem to dominate the return except at the fourth peak near 23 MHz. In general, the first and second peaks show more persistence with scattering and polarization diversity. For a closer look at the scattering pattern of the highest mode, Figure 3 shows that its E-field strength in the *HH-pol* channel is enhanced in the forward direction, with the maximum in the scattering direction $\varphi_{scat} = 180°$ for incident direction $\varphi_{inc} = 0°$. The forward to backward ratio becomes lowest for the incident angle $\varphi_{inc} = -90°$ and highest for the incident angle $\varphi_{inc} = 90°$. In the *VH-pol* channel, the oblique incident angle $\varphi_{inc} = 45°$ has maximal return in the scattering direction $\varphi_{scat} = -90°$, whereas the fourth mode return diminishes in the backward direction for

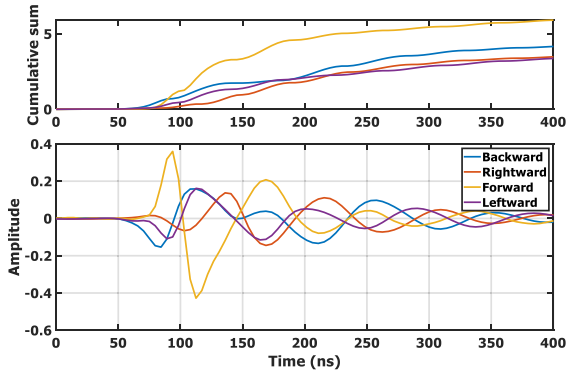

(a) HH-pol

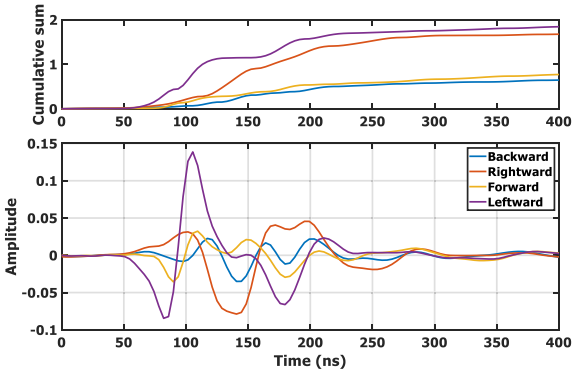

(b) VH-pol

FIGURE 5. Noise-free time response per scattering direction for $\varphi_{\mathbf{inc}} = 45$.

the incident angles $\varphi_{inc} = -90°$ (rear) and 90° (front), as the target shape is symmetrical within the incident plane.

The mode-averaged scattering pattern, as depicted in Figure 4, gives the scattering pattern per incident direction to show the scattering directions with maximal mode-averaged strength. For the *HH-pol* channel, the forward directions near $\varphi_{scat} = [180, 135, -135°]$ of the incident angles $\varphi_{inc} = [0, -45, 45°]$, respectively, have maximal mode strength in descending order. Additionally, the oblique incident angles $\varphi_{inc} = [-45, +45°]$ show several local maxima, notably within their side scattering directions. For the *VH-pol* channel, the oblique incident angle $\varphi_{inc} = +45°$ has two maxima near the scattering directions $\varphi_{scat} = [-90, 180°]$. Hence, the broadside and oblique incident angles have better mode-averaged scattering.

B. TIME-DOMAIN ANALYSIS (COHERENT DATA)

For model A, Figure 5 depicts an example of noise-free time data (inset: cumulative sum (CS)) for the incident direction $\varphi_{inc} = 45°$. The cumulative sum curve ascends faster in the early time and then converges notably quicker in the *VH-pol* channel. Individually, the forward and leftward scattering directions of the *HH-pol* and *VH-pol* channels, sequentially, have the highest cumulative sums, i.e., average power. In comparison to the backward direction, the forward and side scattering directions have reduced specular return and enhanced transient return.

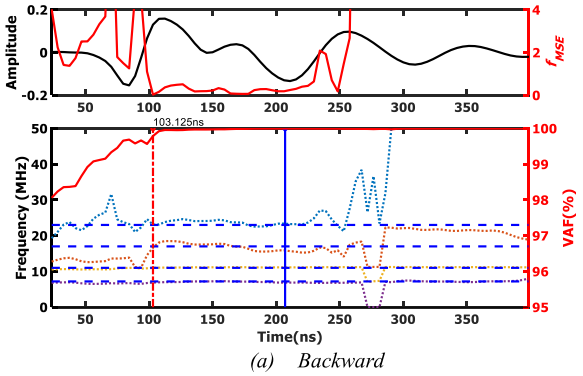

(a) Backward

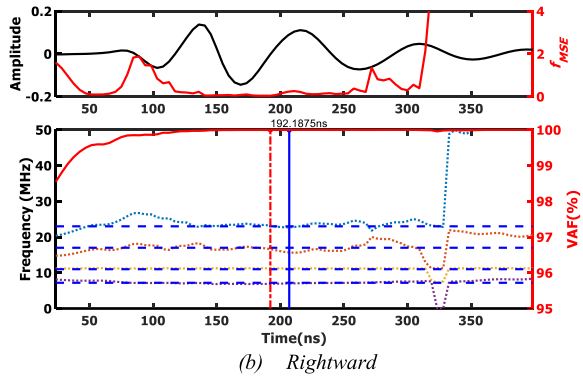

(b) Rightward

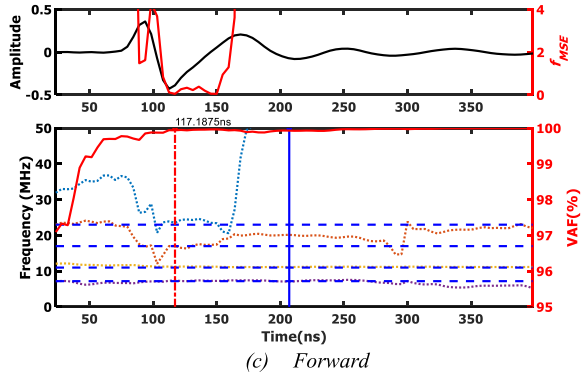

(c) Forward

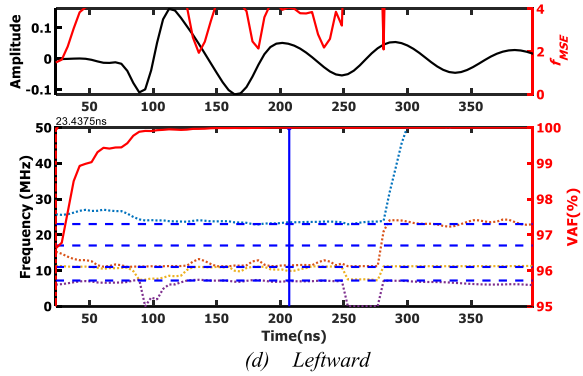

(d) Leftward

FIGURE 6. Model A, noise-free mode frequency distribution versus onset within the *HH-pol* channel for $\varphi_{\mathbf{inc}} = 45$ (reference frequencies (horizontal dashed blue lines), nominal onset (vertical dashed-dotted red line), and reference onset (vertical blue line)).

To gain more insights into the onset impact, Figure 6 (inset: left axis (truncated signal) and right axis (f_{MSE}) limited to 4 MHz^2) shows the fourth-order mode frequency

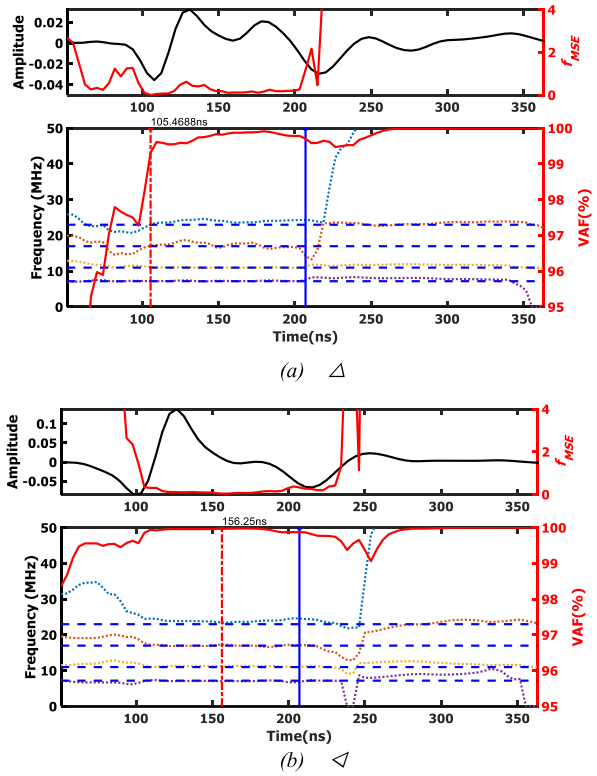

FIGURE 7. The mode frequency distribution versus onset within the *VH*-pol channel given φ_{inc} =45°. (a) forward and (b) leftward.

distribution (left axis) and *VAF* (right axis) versus onset for a window of $\Delta T_L = 23$ to 400 ns in the *HH-pol* channel. The reference onset, represented by the blue vertical line, is approximately 210 ns, for which the first magnitude spectrum peak occurs at approximately 7.14 MHz, as in the *HH-pol* spectrum, i.e., $1/f_1' = 140$ ns. Expansion of the minimal onset bin, ΔT_{MSE}, should help reduce the ambiguity impact, as it becomes feasible to extract the mode frequency more robustly at onsets before or after the reference onset. In Figure 6, the rightward direction shows the most extended bin, while the forward and leftward directions have the smallest bin, mostly affecting the robustness (accuracy and consistency) of the third and fourth modes.

In Figure 6, the minimum error onset, i.e., T_{MSE}, always occurs before the reference onset, signifying that the modes may evolve earlier due to the low-resolution excitation aided by the bistatic scattering and polarization diversity.

Figure 7 demonstrates the positive impact of the *VH*-pol on the third and fourth modes in the forward and leftward scattering directions as seen by their extended onset bins. Note that since the damping and dominance factors fluctuate with direction, we cannot choose a reference value for them to check the accuracy. However, we can exclude spurious values by implementing a limit on the extracted poles (frequency and damping factor.)

Next, Table 2 quantifies the *VH*-pol channel impact based on the four factors of interest, i.e., f_{MSE}, T_{MSE}, ΔT_{MSE} and VAF_{MSE}, demonstrating that the two incident angles φ_{inc}=[0,45°] are the most likely incident directions able to

TABLE 2. The F_{MSE}, T_{MSE}, ΔT_{MSE} and VAF_{MSE} of ϕ_{INC} =[−45,0,45,90] in the VH-pol channel.

	$f_{MSE}(MHz^2)$	$T_{MSE}(ns)$	$\Delta T_{MSE}(ns)$	$VAF_{MSE}(\%)$
Directions	φ_{inc}=-45			
▽	0.09	230.47	97.66	99.98
▷	0.06	152.34	50.78	99.83
△	10.46	82.03	0.00	96.61
◁	0.08	253.91	160.16	99.89
	φ_{inc}=90			
▽	220.04	32.81	0.00	13.80
▷	0.01	23.44	32.81	97.25
△	154.04	56.25	0.00	8.89
◁	0.01	23.44	32.81	97.25
	φ_{inc}=0			
▽	0.04	257.81	131.25	99.96
▷	0.05	262.50	135.94	99.99
△	0.08	239.06	178.13	99.92
◁	0.02	121.88	164.06	99.81
	φ_{inc}=45			
▽	0.01	175.78	97.66	99.69
▷	0.01	183.59	54.69	99.95
△	0.00	105.47	136.72	99.32
◁	0.04	156.25	128.91	99.97

reduce the onset ambiguity because of their low f_{MSE} and high ΔT_{MSE}.

The backward and forward directions of the incident angle $\varphi_{inc} = 90°$ fail to extract any mode in the *VH-pol* channel since the cross-polarized component becomes negligible due to the symmetry of the target in the radar line of sight. For other directions, the *VAF* is almost 100%, but this only indicates that there is sufficient signal energy to extract any existing mode in the truncated signal and does not guarantee the existence of all modes.

Figure 8 confirms that the poles of the optimum onset, namely, the optimal poles, of the incident directions φ_{inc} =[0,45°] have a considerable degree of resemblance to the poles of the reference onset, namely, the reference poles,

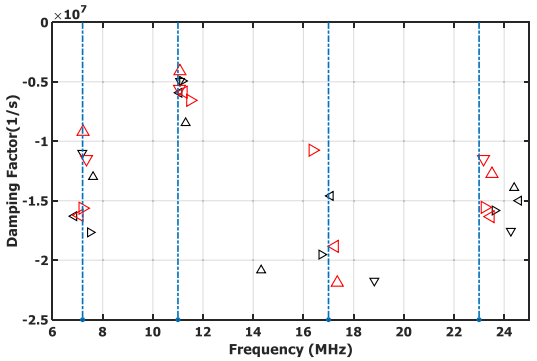

(a) φ_{inc}=45°

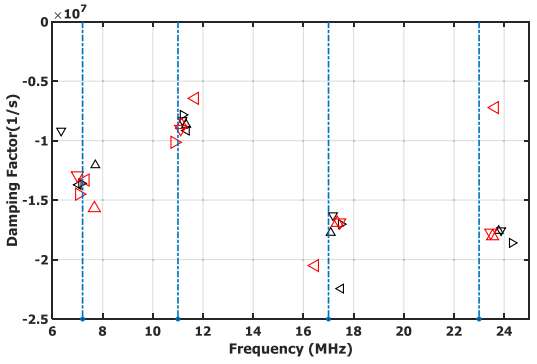

(b) φ_{inc}=0°

FIGURE 8. The damping factor distribution per direction for the *VH-pol* channel given the reference (black) and optimal (red) onsets. (Vertical dashed-dotted lines indicate reference frequencies.)

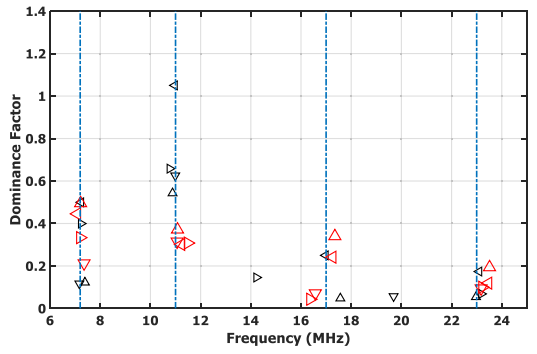

(a) φ_{inc}=45°

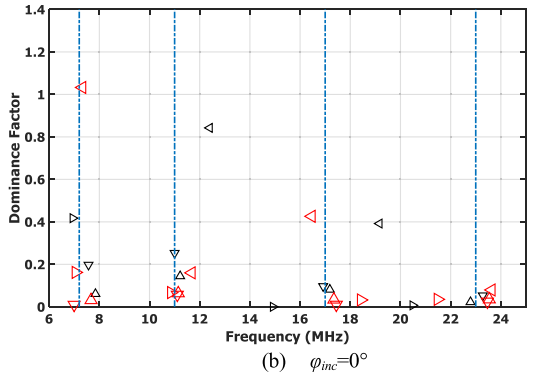

(b) φ_{inc}=0°

FIGURE 9. The dominance factor of models A (red) and B (black) for the *VH-pol* channel given (a) φ_{inc} =45° and (b) φ_{inc} =0°.

especially the first and second poles. In general, for the first and third modes, the incident direction $\varphi_{inc} = 0°$ shows better

TABLE 3. The F_{MSE}, T_{MSE}, ΔT_{MSE} and VAF_{MSE} per SNR for $N_P = 1000$ *in the VH-pol* channel.

Direction	$f_{MSE}(MHz^2)$	$T_{MSE}(ns)$	$\Delta T_{MSE}(ns)$	$VAF_{MSE}(\%)$
	0 dB			
▽	*0.10*	*175.78*	*85.94*	*98.54*
▷	*1.02*	*125.00*	*54.69*	*99.57*
△	*0.01*	*105.47*	*144.53*	*98.91*
◁	*0.04*	*234.38*	*148.44*	*96.56*
	-10 dB			
▽	*1.14*	*125.00*	*54.69*	*94.94*
▷	*2.62*	*97.66*	*42.97*	*98.51*
△	*0.06*	*105.47*	*62.50*	*95.43*
◁	*0.35*	*113.28*	*19.53*	*98.73*
	-20 dB			
▽	*373.99*	*101.56*	*0.00*	*68.21*
▷	*8.31*	*50.78*	*0.00*	*93.20*
△	*9.46*	*74.22*	*0.00*	*76.71*
◁	*12.88*	*54.69*	*0.00*	*96.46*

clustering of poles per scattering direction than the incident direction $\varphi_{inc} = 45°$, where most of the deviation comes from the decay factor as a result of the early time inclusion.

Figure 9 compares the dominance factors of the two models to illustrate the influence of the wing down-sweep on the modes, mainly the second mode dominance. In this respect, the incident angle $\varphi_{inc} = 45°$ displays better clustering for both models, but the leftward direction of the second frequency reflects most of the change impact, as its optimal dominance lies farthest from the reference one.

In terms of direction dominance, the forward and leftward directions of the incident angle $\phi_{inc} = 45°$ are the most dominant, while the backward direction seemingly never becomes dominant. The four factors listed in Table 3 for signal-to-noise ratios of SNR=[0, −10, −20 dB] quantify the consequence of additive white Gaussian noise (AWGN) on the modes with interpulse integration, CIT=0.5 ms. The factors show that the onset effect can be reasonably mitigated down to −10 dB for one run (simulation) of 1000 interpulse integration.

However, as compensation for lowering the SNR level, the optimal onset shifts further towards earlier times to include more of the early-time energy and, in doing so, increase the energy of the truncated signal.

For the signal-to-noise ratio SNR=−20 dB, the corresponding dominance distribution, displayed in Figure 10, shows nineteen spurious poles above 24 MHz and twelve poles below this value, of which eight are optimal and four are reference poles. Hence, the extraction with the optimal onset is 100% better than that with the reference onset, which

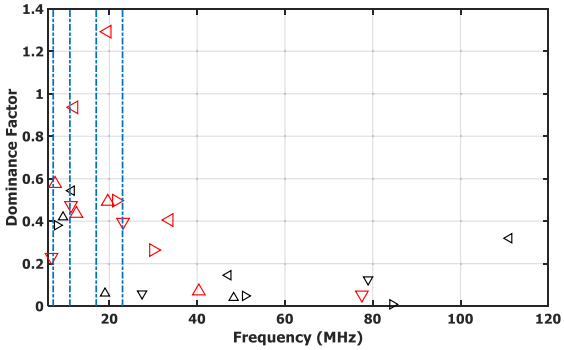

FIGURE 10. One simulation of the integrated dominance factor within the VH-pol channel given SNR=−20 dB.

reflects the degree of impact that the minimum onset has on the estimation of the modes.

V. CONCLUSION

The conducted approach presents a qualitative assessment of both the frequency (noncoherent) and time (coherent) data and has successfully determined the optimum onset solely based on the radar echo signal and proved its dependency on the bistatic scattering and polarization radar configurations. The preliminary evaluation in the frequency domain derived reference (ideal) mode frequencies from the magnitude spectrum peak frequencies, and their scattering pattern predicted those bistatic directions of enhanced mode return. Then, in the time domain, the minimum frequency error gave the optimal onset bin and its optimum onset and with the *VAF* factor formed the four robustness factors, i.e., f_{MSE}, T_{MSE}, ΔT_{MSE} and VAF_{MSE}, to find those bistatic and polarization configuration(s) of robust modes. Mainly, the optimal onsets in these robust bistatic and polarization configurations improved the higher-order modes that are usually very sensitive to the onset shift in a monostatic case. This paper utilized two models of same-class aircraft targets to validate the improvement with the optimum onset in the context of radar target identification, where the dominance distribution had a better chance of discriminating the two models with the optimum onset than with the reference onset. Under noise perturbation, the dominance distribution pertaining to the optimum onset was estimated more robustly compared to that pertaining to the reference onset.

REFERENCES

[1] F. Aldhubaib, "Generic aircraft model recognition by two shape factors: In the resonance region," *IET Radar, Sonar Navigat.*, vol. 14, no. 1, pp. 81–88, Jan. 2020, doi: 10.1049/iet-rsn.2019.0089.

[2] Y. Ma, L. Zhu, and Y. Li, "HRRP-based target recognition with deep contractive neural network," *J. Electromagn. Waves Appl.*, vol. 33, no. 7, pp. 911–928, May 2019.

[3] J. Liu and B. F. Wang, "Dynamic aircraft identification using HRRP under attitude perturbation interference," *J. Electromagn. Waves Appl.*, vol. 33, no. 7, pp. 929–945, May 2019.

[4] F. Aldhubaib, "Binary Stokes vector representation of aircraft in the low-resolution radar context," *IET Radar, Sonar Navigat.*, vol. 13, no. 11, pp. 2041–2045, Nov. 2019.

[5] I.-H. Kim, I.-S. Choi, and D.-Y. Chae, "A study on the performance enhancement of radar target classification using the two-level feature vector fusion method," *J. Electromagn. Eng. Sci.*, vol. 18, no. 3, pp. 206–211, Jul. 2018, doi: 10.26866/jees.2018.18.3.206.

[6] S.-J. Lee, I.-S. Choi, B. Cho, E. J. Rothwell, and A. K. Temme, "Performance enhancement of target recognition using feature vector fusion of monostatic and bistatic radar," *Prog. Electromagn. Res.*, vol. 144, pp. 291–302, 2014. [Online]. Available: http://www.jpier.org/PIER/pier.php?paper=13103101, doi: 10.2528/PIER13103101.

[7] W. C. Chen and N. V. Z. Shuley, "Robust target identification in white Gaussian noise using canonical correlation analysis," *IEEE Trans. Antennas Propag.*, vol. 60, no. 7, pp. 3533–3537, Jul. 2012, doi: 10.1109/TAP.2012.2196939.

[8] C. E. Baum, E. J. Rothwell, K.-M. Chen, and D. P. Nyquist, "The singularity expansion method and its application to target identification," *Proc. IEEE*, vol. 79, no. 10, pp. 1481–1492, 1991.

[9] C. E. Baum, "Signature-based target identification and pattern recognition," *IEEE Antennas Propag. Mag.*, vol. 36, no. 3, pp. 44–51, Jun. 1994.

[10] C. E. Baum, "Signature based target recognition," Res. Technol. Org., Paris, France, Tech. Rep. AC/323 (SET) TP/1, 1998.

[11] C. Baum, "Combining polarimetry with SEM in radar backscattering for target identification," in *Proc. 3rd Int. Conf. Ultrawideband Ultrashort Impulse Signals*, Sevastopol, Ukraine, Sep. 2006, pp. 18–22.

[12] T. K. Sarkar and O. Pereira, "Using the matrix pencil method to estimate the parameters of a sum of complex exponentials," *IEEE Antennas Propag. Mag.*, vol. 37, no. 1, pp. 48–55, Feb. 1995.

[13] D. Q. Liu, H. Li, H. G. Wang, and D. Yang, "Multi-GPOF method in the calculation of the rectangular waveguide layered Green's functions," *IEEE Antennas Wireless Propag. Lett.*, vol. 9, pp. 1143–1147, 2010, doi: 10.1109/LAWP.2010.2096795.

[14] H. Nazli and A. A. Ergin, "Application of the generalized pencil of function method to time reversal imaging," *IEEE Antennas Wireless Propag. Lett.*, vol. 16, pp. 3113–3117, 2017, doi: 10.1109/LAWP.2017.2763959.

[15] S. Ur Rehman and M. A. S. Alkanhal, "System modelling and synthesis of stepped impedance resonators and filters," *IET Microw., Antennas Propag.*, vol. 13, no. 15, pp. 2693–2700, Dec. 2019, doi: 10.1049/iet-map.2018.5772.

[16] E. Rothwell, K.-M. Chen, D. Nyquist, and W. Sun, "Frequency domain E-pulse synthesis and target discrimination," *IEEE Trans. Antennas Propag.*, vol. 35, no. 4, pp. 426–434, Apr. 1987, doi: 10.1109/TAP.1987.1144116.

[17] E. J. Rothwell, K.-M. Chen, D. P. Nyquist, P. Ilavarasan, J. E. Ross, R. Bebermeyer, and Q. Li, "A general E-pulse scheme arising from the dual early-time/late-time behavior of radar scatterers," *IEEE Trans. Antennas Propag.*, vol. 42, no. 9, pp. 1336–1341, 1994, doi: 10.1109/8.318656.

[18] Q. Li, P. Ilavarasan, J. E. Ross, E. J. Rothwell, K.-M. Chen, and D. P. Nyquist, "Radar target identification using a combined early-time/late-time E-pulse technique," *IEEE Trans. Antennas Propag.*, vol. 46, no. 9, pp. 1272–1278, Sep. 1998.

[19] C. O. Hargrave, I. V. L. Clarkson, and H.-S. Lui, "Late-time estimation for resonance-based radar target identification," *IEEE Trans. Antennas Propag.*, vol. 62, no. 11, pp. 5865–5871, Nov. 2014, doi: 10.1109/TAP.2014.2350507.

[20] F. F. H. Aldhubaib and N. V. Z. Shuley, "Characteristic polarization states estimation in an ultrawideband context: A frequency approach," *IEEE Trans. Geosci. Remote Sens.*, vol. 47, no. 8, pp. 2808–2817, Aug. 2009, doi: 10.1109/TGRS.2009.2014564.

[21] F. Aldhubaib, "Impact of onset ambiguity on SEM signature and reduction approach by scattering and polarization diversification," *J. Electromagn. Anal. Appl.*, vol. 12, no. 03, pp. 29–42, 2020.

[22] *Feko Suite 7.0*, Altair, Stellenbosch, South Africa, 2014.

[23] F. Aldhubaib, N. V. Shuley, and H. S. Lui, "Characteristic polarization states in an ultrawideband context based on the singularity expansion method," *IEEE Geosci. Remote Sens. Lett.*, vol. 6, no. 4, pp. 792–796, Oct. 2009, doi: 10.1109/LGRS.2009.2025611.

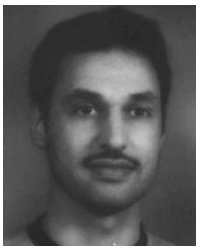

FAISAL F. H. ALDHUBAIB received the B.E. and M.Sc. degrees in electrical engineering from the University of Leeds, U.K., in 1995 and 1997, respectively, and the Ph.D. degree with the Electromagnetic and Imaging Research Group, School of Information Technology and Electrical Engineering (ITEE), University of Queensland, Australia, in 2009. He has been an Assistant Professor with the Department of Electronic Engineering Technology, College of Technological Studies, Kuwait, since 2010. His current research interests include polarimetric and resonance-based target recognition techniques.